Applied Catalysis A: General 521 (2016) 9–18

Contents lists available at ScienceDirect

Applied Catalysis A: General

journal homepage: www.elsevier.com/locate/apcata

Enhancement of the Cr(VI) adsorption and photocatalytic reduction activity of g-C_3N_4 by hydrothermal treatment in HNO_3 aqueous solution

Hongtao Wei [a], Qian Zhang [b], Yongcai Zhang [b,*], Zhanjun Yang [b], Aiping Zhu [b], Dionysios D. Dionysiou [c,*]

[a] College of Chemistry and Pharmaceutical Science, Qingdao Agricultural University, Qingdao 266109, China
[b] Jiangsu Key Laboratory of Environmental Material and Environmental Engineering, School of Chemistry and Chemical Engineering, Yangzhou University, Yangzhou 225002, China
[c] Environmental Engineering and Science Program, Department of Biomedical, Chemical and Environmental Engineering, 705 Engineering Research Center, University of Cincinnati, Cincinnati, OH 45221-0012, USA

ARTICLE INFO

Article history:
Received 3 August 2015
Received in revised form 31 October 2015
Accepted 3 November 2015
Available online 10 November 2015

Keywords:
Graphitic carbon nitride
Hydrothermal treatment
Adsorption
Photocatalytic reduction
Hexavalent chromium

ABSTRACT

An effective and environmental-friendly method was adopted to enhance the Cr(VI) adsorption and photocatalytic reduction activity of g-C_3N_4, which was prepared by thermal condensation of melamine. The enhancement was realized by hydrothermal treatment of g-C_3N_4 in 1.9–7.6 mol/L HNO_3 aqueous solutions at 80–120 °C for 3–12 h. The compositions, structures and physiochemical properties of the hydrothermally treated g-C_3N_4 were characterized by X-ray diffraction, X-ray photoelectron spectroscopy, Fourier transform infrared spectroscopy, scanning electron microscopy, transmission electron microscopy, N_2 adsorption/desorption isotherms, Zeta potential analysis, UV–vis diffuse reflectance spectroscopy and photocurrent measurement, and their dark adsorption and visible-light (wavelength >420 nm)-driven photocatalytic reduction of Cr(VI) in aqueous solution were tested. It was found that the hydrothermally treated g-C_3N_4 exhibited significantly enhanced Cr(VI) adsorption and photocatalytic reduction activity than g-C_3N_4. Moreover, larger concentration of HNO_3 aqueous solution, higher hydrothermal temperature or longer treatment time resulted in higher Cr(VI) adsorption and photocatalytic reduction activity of the hydrothermally treated g-C_3N_4. The reasons accounting for the enhanced Cr(VI) adsorption and photocatalytic reduction activity of the hydrothermally treated g-C_3N_4 were discussed, and the different mechanisms for the photocatalytic reduction of Cr(VI) over g-C_3N_4 and the hydrothermally treated g-C_3N_4 were also proposed.

1. Introduction

Hexavalent chromium (Cr(VI)) is a troublesome pollutant in the effluents from chromate-related industries, such as mining, chromate production, electroplating, leather tanning, pigment, and wood preservation. Cr(VI) has high toxicity and high solubility and mobility in water, and can do great harm to the environment and human health [1–3]. Therefore, it is necessary to explore effective, economical, and environmental-friendly methods for the treatment of wastewater contaminated with Cr(VI) [4–6]. Semiconductor mediated photocatalytic reduction is a promising method for treating Cr(VI) contaminated wastewaters, because this treatment method has many distinguished characteristics [7–14]: (i) effectiveness (the Cr(VI) concentration after photocatalytic reduction can be reduced up to the detection limit of the diphenylcarbazide colorimetric method, 0.005 mg/L [14], which is much lower than the allowable limit of Cr(VI) in drinking water proposed by the World Health Organization, 0.05 mg/L), (ii) good ability to directly utilize solar energy, (iii) no secondary pollution, and less release of sludge than the traditional iron and $FeSO_4$ reduction methods, (iv) reusability, (v) low cost, and (vi) the reduced product, Cr(III) has only about one percent toxicity of that of Cr(VI), and is easy to be precipitated in aqueous solution ($K_{sp}^{y}(Cr(OH)_3) = 6.3 \times 10^{-31}$) and disposed as a sludge [14]. Nonetheless, for the practical application of photocatalysis technology in treating Cr(VI) contaminated wastewaters, it should be a premise to research for efficient visible-light-active photocatalysts.

* Corresponding authors.
E-mail addresses: zhangyc@yzu.edu.cn (Y. Zhang), dionysdd@ucmail.uc.edu (D.D. Dionysiou).

http://dx.doi.org/10.1016/j.apcata.2015.11.005
0926-860X/

Graphite-like carbon nitride (g-C_3N_4) is a metal-free polymer semiconductor, having a medium bandgap of approximately 2.7 eV [15]. It is nontoxic and has good chemical stability, and can be easily synthesized from abundant and cheap CN-containing precursors [16–20]. Moreover, it has been proved to possess visible-light-driven photocatalytic activity for many chemical reactions [21–28]. Thus, g-C_3N_4 holds great promise as a visible-light-active photocatalyst for industrial applications. However, the g-C_3N_4 synthesized via the traditional thermal condensation methods exhibited low photocatalytic activity, because of its large particles size, severe aggregation, and small specific surface area [29–43]. Hence, many researchers have now turned to devise various modification strategies to improve the photocatalytic activity of g-C_3N_4 [29–43]. The effective modification methods developed for g-C_3N_4 photocatalyst included copolymerization [29], doping [30,31], texturization [32–35], supermolecular assembly [36], surface heterojunction [37–39], and acid treatment [40–43], etc.

Acid treatment is a simple and effective way for improving the multiple performance of g-C_3N_4 [40–43]. For example, Zhang et al. reported that the protonation of g-C_3N_4 with HCl can not only enhance its ionic conductivity and photoconduction, but also enable the preparation of other promising g-C_3N_4 based hybrid composites by counteranion exchange [40]. Zhang et al. reported that the chemical protonation of graphitic carbon nitride (CN) solids with strong oxidizing HNO_3 was efficient in the sol processing of a stable CN colloidal suspension, which can be converted to thin films with enhanced photo-electrochemical performance by dip/disperse-coating techniques [41]. Xu et al. reported that the single atomic layer g-C_3N_4 nanosheets produced via sonicated chemical exfoliation of bulk g-C_3N_4 in H_2SO_4 aqueous solution exhibited higher photocatalytic activity in H_2 production and pollutant decomposition [42]. We also reported that the photocatalytic activity of g-C_3N_4 in the reduction of aqueous Cr(VI) under visible-light (wavelength >420 nm) irradiation can be improved simply by soaking g-C_3N_4 in 5 mol/L HNO_3 or HCl aqueous solution for 2 h at room temperature [43]. However, the improvement in the photocatalytic activity of g-C_3N_4 was only small, and the underlying mechanism was not comprehensively expounded in the preliminary study [43]. Furthermore, HNO_3 or HCl was prone to volatilize during the acid treatment process in air.

Herein, for the sake of further enhancing the photocatalytic activity of g-C_3N_4 and also avoiding the volatilization of HNO_3 during the acid treatment process, we conducted the HNO_3 treatment of g-C_3N_4 in the sealed autoclave under hydrothermal conditions. The effects of the HNO_3 concentration, hydrothermal temperature and treatment time on the Cr (VI) adsorption and photocatalytic reduction activity of the hydrothermally treated g-C_3N_4 were investigated. The reasons accounting for the enhanced Cr(VI) adsorption and photocatalytic reduction activity of the hydrothermally treated g-C_3N_4 were discussed, and the different mechanisms for the photocatalytic reduction of Cr(VI) over g-C_3N_4 and the hydrothermally treated g-C_3N_4 were also proposed.

2. Experimental

2.1. Synthesis of g-C_3N_4

An amount of melamine (3000 mg) was placed into a 50 mL corundum crucible and covered with a lid. They were then heated in a program control chamber electric furnace from room temperature to 520 °C at a heating rate of 4 degrees per minute, further maintained at 520 °C for 4 h, afterwards cooled to room temperature naturally. The residual solid was collected and ground into powder. The as-obtained sample was denoted as g-C_3N_4.

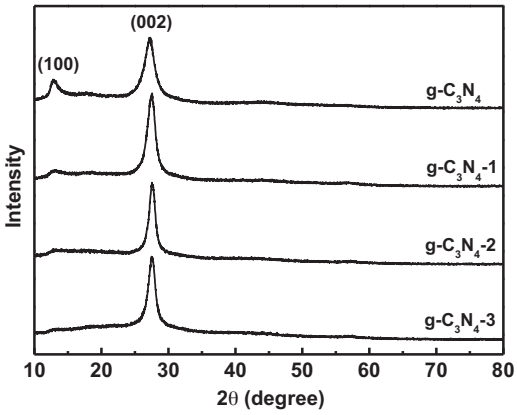

Fig. 1. XRD patterns of g-C_3N_4, g-C_3N_4-1, g-C_3N_4-2 and g-C_3N_4-3.

2.2. Hydrothermal treatment of g-C_3N_4

500 mg of g-C_3N_4 was put into a 50 mL Teflon jar, and 40 mL of 1.9, 5.0 or 7.6 mol/L HNO_3 aqueous solution was added and stirred for 20 min. The mixture was sealed into stainless steel autoclave and heated at 80–120 °C for 3–12 h. After the autoclave cooled down to room temperature naturally, the resulting powder was centrifuged, washed with deionized water and absolute ethanol, and dried in air at 100 °C for 4 h.

2.3. Characterization

The samples were characterized by XRD (Bruker AXS D8 ADVANCE X-ray diffractometer), FTIR (Varian Cary 670 FT-IR spectrometer), XPS (Thermo-VG Scientific ESCALAB 250 XPS system, Al Kα radiation and adventitious C 1s peak (284.8 eV) calibration), SEM (Hitachi S-4800 Field Emission Scanning Electron Microscopy), TEM (FEI Tecnai G^2 F30 S-TWIN field-emission transmission electron microscopy), N_2 adsorption/desorption isotherms (Micromeritics Instrument Corporation TriStar II 3020 surface area and porosity analyzer), Zeta potential analyzer (Malvern Instruments Zetasizer Nano ZS90) and UV–vis diffuse reflectance spectra (Varian Cary 5000 UV–vis-NIR spectrophotometer). The photocurrent response was measured on a CHI-660D electrochemical workstation (Beijing Chinese Science Days Technology Co., Ltd.) using a standard three-electrode cell. A 23 W Philips Energy Saver Light Bulb provided the visible-light irradiation.

2.4. Adsorption and photocatalytic reduction of Cr(VI)

The experiments were carried out in our custom-made photochemical reactor [43]. Before illumination, 300 mL of 50 mg/L $K_2Cr_2O_7$ aqueous solution, 1.0 mL of 100 mg/mL citric acid aqueous solution and 300 mg of photocatalyst were mixed (the pH of the mixture was 3.1, which was the optimum pH value among 1.0, 2.0, 3.1, 5.0 and 7.0 to achieve the highest efficiency of Cr(VI) adsorption and photocatalytic reduction) and magnetically stirred for 60 min to ensure the Cr(VI) adsorption equilibrium. During illumination by visible-light (wavelength >420 nm), nearly 4 mL of suspension was taken from the reactor at a scheduled time interval and filtered with cellulose acetate membrane (pore size was 0.22 μm) to separate the photocatalyst. The Cr(VI) contents in the filtrates were determined using the diphenylcarbazide colorimetric method [43].

3. Results and discussion

For the convenience of description, the samples derived from hydrothermal treatment of g-C_3N_4 in 1.9, 5.0 and 7.6 mol/L of HNO_3

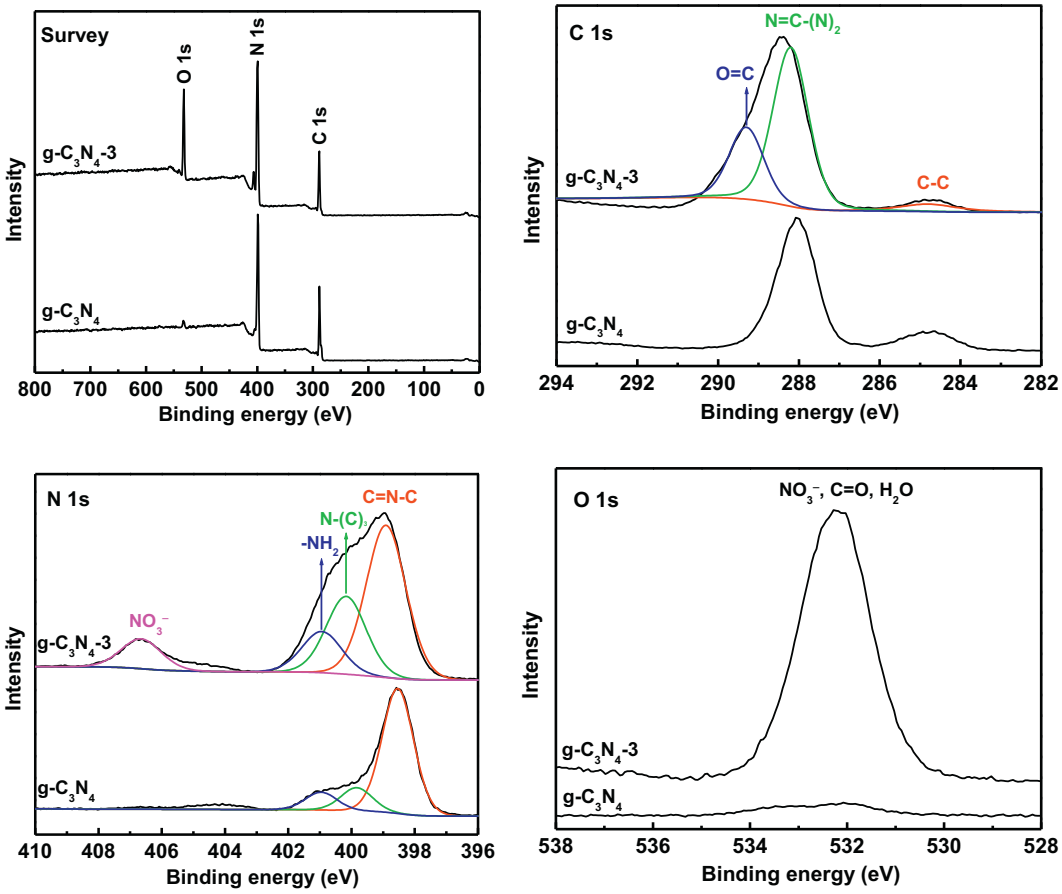

Fig. 2. XPS spectra of g-C_3N_4 and g-C_3N_4-3.

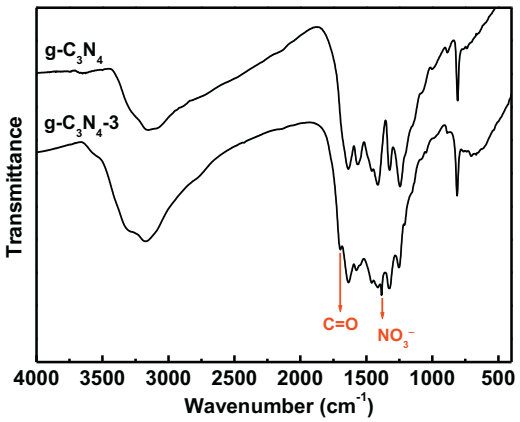

Fig. 3. FTIR spectra of g-C_3N_4 and g-C_3N_4-3.

aqueous solution at 120 °C for 12 h are hereinafter abbreviated as g-C_3N_4-1, g-C_3N_4-2 and g-C_3N_4-3, respectively. Fig. 1 shows the XRD patterns of g-C_3N_4-1, g-C_3N_4-1 and g-C_3N_4-3. As can be seen from Fig. 1, g-C_3N_4 displayed two typical XRD peaks of graphite-like carbon nitride at about 12.9° and 27.2°. The XRD peak at 12.9° corresponded to the in-plane structural packing motif of the conjugated aromatic systems and can be indexed as the (100) crystal plane of g-C_3N_4; whereas the XRD peak at 27.2° corresponded to the interplanar stacking of the conjugated aromatic systems and can be indexed as the (002) crystal plane of g-C_3N_4 [43–45]. The XRD patterns of g-C_3N_4-1, g-C_3N_4-2 and g-C_3N_4-3 still contained the characteristic (002) interlayer-stacking peak, suggesting the graphite-like structure of g-C_3N_4 was still retained after the hydrothermal treatment in 1.9–7.6 mol/L HNO_3 aqueous solutions at 120 °C for 12 h. Nevertheless, it seemed that the (002) peak of g-C_3N_4-1, g-C_3N_4-2 and g-C_3N_4-3 turned sharpening, as compared with that of g-C_3N_4. This might be because the unstable domains of not-well-ordered carbon nitride had been removed after the hydrothermal treatment in 1.9–7.6 mol/L HNO_3 aqueous solutions at 120 °C for 12 h [20]. Besides, the (100) peak of g-C_3N_4 became much weaker in the XRD pattern of g-C_3N_4-1 or almost disappeared in the XRD patterns of g-C_3N_4-2 and g-C_3N_4-3. This was likely because the in-plane periodic arrangement of the conjugated aromatic segments of g-C_3N_4 had been destroyed after the hydrothermal treatment in HNO_3 aqueous solutions. Furthermore, the yields of g-C_3N_4-1, g-C_3N_4-2 and g-C_3N_4-3 were 89.6%, 61.9% and 24.6%, respectively, with reference to the starting amount of g-C_3N_4 used for the hydrothermal treatment. Thus, it can be inferred that during the hydrothermal treatment in HNO_3 aqueous solutions, the oxidation etching and protonation depolymerization of g-C_3N_4 had occurred [41]. Moreover, larger concentration of HNO_3 aqueous solution can cause more oxidation etching and protonation depolymerization of g-C_3N_4.

The surface elemental composition and chemical states of g-C_3N_4 and g-C_3N_4-3 were analyzed by XPS. The survey XPS spectra in Fig. 2 revealed that both samples contained C, N and O. The C 1s XPS spectrum of g-C_3N_4 displayed two peaks at (i) 284.8 eV and (ii) 288.2 eV (Fig. 2), which can be assigned to (i) graphite and adventitious C and (ii) sp^2-bonded C in N-containing aromatic rings (N—C═N) [46–49], respectively. By contrast, the C 1s XPS spectrum of g-C_3N_4-3 can be deconvoluted into three peaks at (i) 284.8 eV, (ii) 288.2 eV and (iii) 289.3 eV (Fig. 2). The two C 1s peaks of g-C_3N_4-3 at 284.8 eV and 288.2 eV were the same as g-C_3N_4. The additional C 1s peak of g-C_3N_4-3 at 289.3 eV can be attributed to C═O [49],

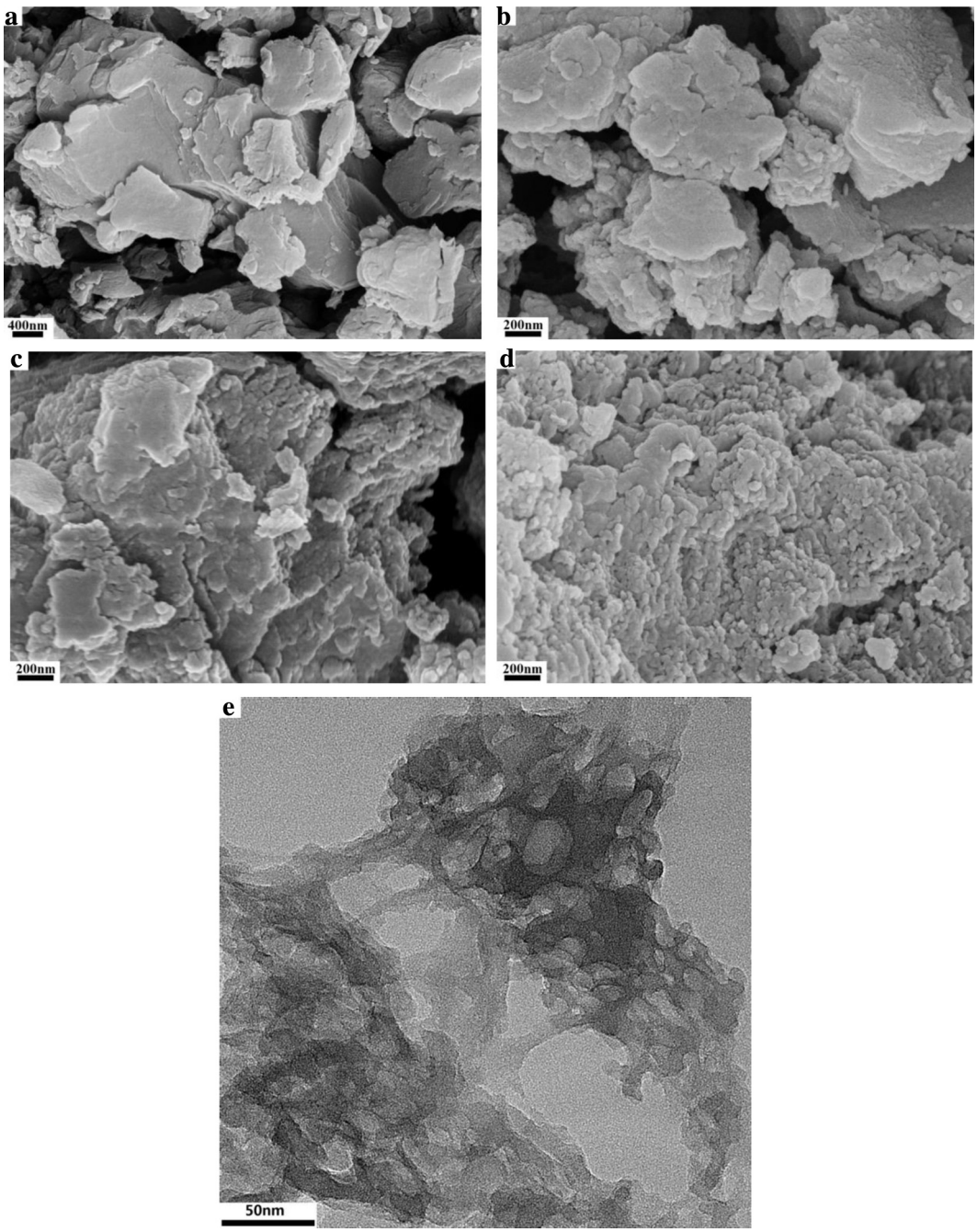

Fig. 4. SEM images of (a) g-C_3N_4, (b) g-C_3N_4-1, (c) g-C_3N_4-2 and (d) g-C_3N_4-3; and (e) TEM image of g-C_3N_4-3.

which suggested that some carbon of g-C_3N_4 had been oxidized after the hydrothermal treatment in 7.6 mol/L of HNO_3 aqueous solution at 120 °C for 12 h. The N 1s XPS spectrum of g-C_3N_4 can be deconvoluted into three peaks at (i) 398.6 eV, (ii) 399.9 eV and (iii) 401.0 eV, whereas the N 1s XPS spectrum of g-C_3N_4-3 can be deconvoluted into four peaks at (i) 398.9 eV, (ii) 400.2 eV, (iii) 401.0 eV and (iv) 406.7 eV (Fig. 2). The N 1s peak at (i) 398.6–398.9 eV, (ii) 399.9–400.2 eV and (iii) 401.0 eV can be assigned to (i) sp^2-hybridized N in C═N—C, (ii) tertiary N bonded to C in the form of N—$(C)_3$ and (iii) —NH_2 [46–49], respectively. The extra N 1s peak of g-C_3N_4-3 at 406.7 eV can be attributed to the NO_3^- adsorbed by the protonated g-C_3N_4 [49], that is, g-C_3N_4-3 was probably in the form of g-C_3N_4–$H^+NO_3^-$ [40]. Besides, the O 1s XPS spectra indicated that the O 1s peak intensity of g-C_3N_4-3 was much stronger than that of g-C_3N_4 (Fig. 2), suggesting that g-C_3N_4-3 contained more oxygen content than g-C_3N_4. The oxygen content of g-C_3N_4-3 might come from NO_3^-, C═O and adsorbed H_2O [49].

Fig. 3 shows the FTIR spectra of g-C_3N_4 and g-C_3N_4-3. Both samples displayed the typical FTIR absorption peaks of g-C_3N_4, for instance, the absorption peak at around 812 cm^{-1} corresponded to the breathing mode of the triazine units [50–54], the absorption peaks between 1200 and 1700 cm^{-1} belonged to the stretching modes of CN heterocycles [50–54], and the absorption bands from about 3000 to 3500 cm^{-1} represented the uncondensed —NH_2 and surface adsorbed H_2O [50–54]. Nevertheless, g-C_3N_4-3 displayed two additional FTIR absorption peaks at around 1703 and 1387 cm^{-1}, which can be assigned to the stretching mode of C═O [55] and NO_3^- [56], respectively. Thus, the FTIR and XPS analysis results of g-C_3N_4-3 were consistent with each other.

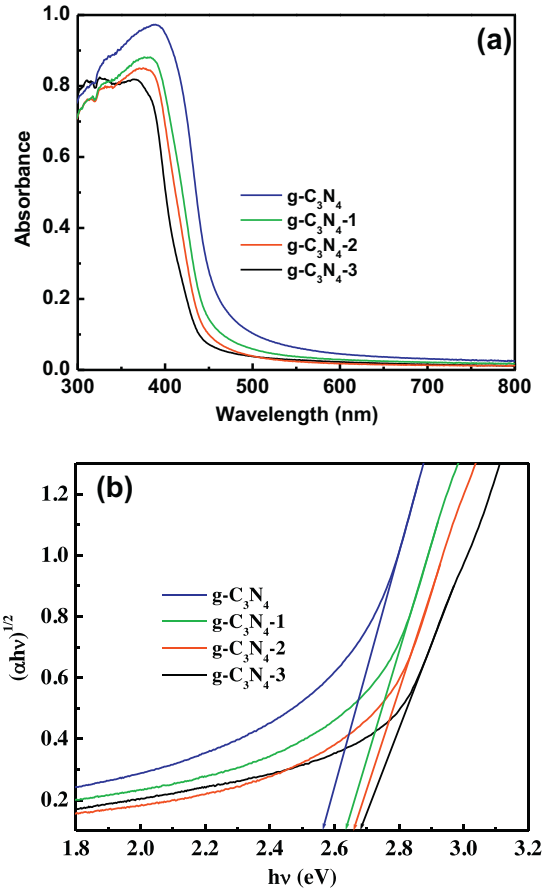

Fig. 5. UV–vis diffuse reflectance spectra of g-C_3N_4, g-C_3N_4-1, g-C_3N_4-2 and g-C_3N_4-3 in the absorbance mode, and (b) Tauc plots for estimating their bandgap (E_g) values.

Fig. 4(a)–(d) show the SEM images of g-C_3N_4, g-C_3N_4-1, g-C_3N_4-2 and g-C_3N_4-3, respectively. It can be seen from Fig. 4(a)–(d) that the particle size of the samples followed an order of g-C_3N_4-3 < g-C_3N_4-2 < g-C_3N_4-1 < g-C_3N_4. This indicated that the particle size of g-C_3N_4 decreased after the hydrothermal treatment in HNO_3 aqueous solution. Moreover, larger concentration of HNO_3 aqueous solution used for the hydrothermal treatment resulted in smaller particle size of g-C_3N_4. Furthermore, the TEM image in Fig. 4(e) revealed that g-C_3N_4-3 comprised porous nanosheets. The smaller porous nanosheets of the hydrothermally treated g-C_3N_4 meant the shorter distance for their photogenerated electrons and holes to migrate from the birth site to the solid-liquid interface, thus reducing the recombination probability of their photogenerated charge carriers [42,50]. The decrease in the particle size and formation of porous nanostructures of the hydrothermally treated g-C_3N_4 may be due to the oxidation etching and protonation depolymerization of g-C_3N_4 during the hydrothermal treatment in HNO_3 aqueous solution. In addition, it was reasonable that larger concentration of HNO_3 aqueous solution can lead to more oxidation etching and protonation depolymerization of g-C_3N_4. This also agreed with the fact that the yields of g-C_3N_4-1, g-C_3N_4-2 and g-C_3N_4-3 were in a descending order.

The BET specific surface areas of g-C_3N_4, g-C_3N_4-1, g-C_3N_4-2 and g-C_3N_4-3 were 1.9, 8.1, 34.9 and 43.4 m^2/g, respectively. This indicated that the specific surface area of g-C_3N_4 had been increased by the hydrothermal treatment in HNO_3 aqueous solution. Moreover, larger concentration of HNO_3 aqueous solution used for the hydrothermal treatment resulted in larger specific surface area of g-C_3N_4. The increased surface area of the hydrothermally treated g-C_3N_4 can provide more surface active sites for the adsorption and photocatalytic reactions [42,50].

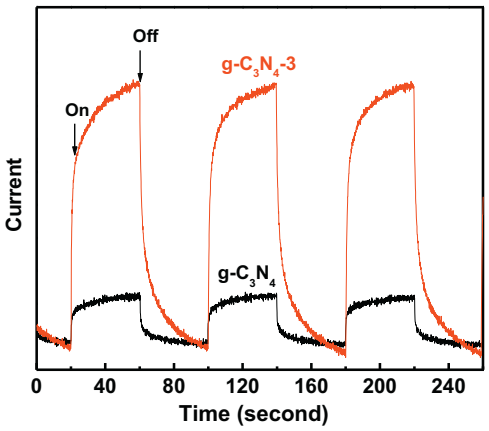

Fig. 6. Photocurrent response of g-C_3N_4 and g-C_3N_4-3 electrodes subjected to the periodic irradiation by 23 W Philips Energy Saver Light Bulb.

The Zeta potentials of g-C_3N_4, g-C_3N_4-1, g-C_3N_4-2 and g-C_3N_4-3 dispersed in water were determined to be −11.9, +48.5, +46.0 and +40.7 mV, respectively. This implied that the hydrothermal treatment in HNO_3 aqueous solution had changed g-C_3N_4 from negative to positive surface charges as a result of protonation [40], which would be beneficial to adsorb more Cr(VI) in the form of mainly $Cr_2O_7^{2-}$ at pH 3.1 through electrostatic attraction [57].

The UV–vis diffuse reflectance spectra of g-C_3N_4, g-C_3N_4-1, g-C_3N_4-2 and g-C_3N_4-3 are shown in Fig. 5(a). As can be observed from Fig. 5(a), the absorption edges of g-C_3N_4-1, g-C_3N_4-2 and g-C_3N_4-3 shifted to shorter wavelength in comparison with that of g-C_3N_4. Moreover, their blue shifts were in the order of g-C_3N_4-3 > g-C_3N_4-2 > g-C_3N_4-1. Using the Tauc plot approach [58–61], the bandgap (E_g) values of g-C_3N_4, g-C_3N_4-1, g-C_3N_4-2 and g-C_3N_4-3 were estimated to be about 2.57, 2.63, 2.66 and 2.68 eV (Fig. 5(b)), respectively. The enlargement in the E_g value of the hydrothermally treated g-C_3N_4 may be due to their smaller porous nanostructures, which can result in quantum confinement effect [41].

Fig. 6 shows the photocurrent response of g-C_3N_4 and g-C_3N_4-3 electrodes subjected to the periodic irradiation by 23 W Philips Energy Saver Light Bulb. The photocurrent response was fast and uniform in each switch-on and switch-off round for both sample electrodes. The photocurrent of g-C_3N_4-3 electrode was far higher than that of g-C_3N_4 electrode, suggesting the much more efficient separation of photogenerated electrons and holes in g-C_3N_4-3 [42,50].

Fig. 7(a) shows the dark adsorption and visible-light (wavelength >420 nm)-driven photocatalytic reduction of Cr(VI) over g-C_3N_4, g-C_3N_4-1, g-C_3N_4-2 and g-C_3N_4-3 in aqueous suspension. As can be observed from Fig. 7(a), the Cr(VI) adsorption capacities of the samples were in the order of g-C_3N_4-3 > g-C_3N_4-2 > g-C_3N_4-1 > g-C_3N_4 (our dark adsorption experiments had demonstrated that the adsorption equilibrium between each sample and Cr(VI) can be achieved after magnetic stirring the mixture of the sample and Cr(VI) aqueous solution for 60 min in the dark). The Cr(VI) adsorption capacities of g-C_3N_4-3, g-C_3N_4-2, g-C_3N_4-1 and g-C_3N_4 were 77.2%, 66.2%, 39.0% and 1.5%, respectively. This indicated that the hydrothermal treatment in HNO_3 aqueous solution can enhance the Cr(VI) adsorption capacity of g-C_3N_4. Moreover, with the increase of the concentration of HNO_3 aqueous solution used for the hydrothermal treatment, the Cr(VI) adsorption capacity of the resultant g-C_3N_4 became larger. After the dark adsorption equilibrium between each sample and Cr(VI), the Cr(VI) concentration continued to decrease once irradiated by visible-light (wavelength >420 nm), suggesting all the samples had visible-light-

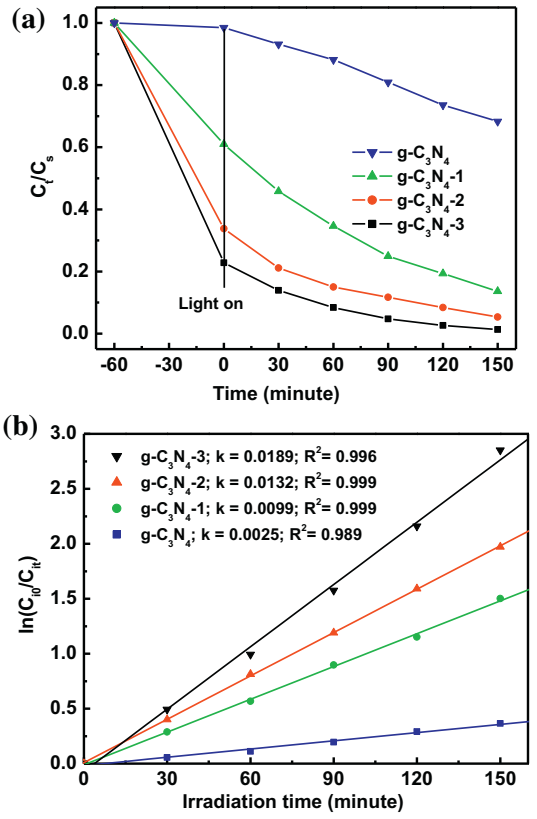

Fig. 7. (a) Dark adsorption and visible-light (wavelength >420 nm)-driven photocatalytic reduction of Cr(VI) over g-C_3N_4, g-C_3N_4-1, g-C_3N_4-2 and g-C_3N_4-3 in aqueous suspension. Note: C_s denotes the starting Cr(VI) concentration in 50 mg/L $K_2Cr_2O_7$ aqueous solution, whereas C_t denotes the Cr(VI) concentration after the dark adsorption or visible-light (wavelength >420 nm) irradiation for t minutes. (b) Plots of $\ln(C_{i0}/C_{it})$ vs irradiation time (t) to obtain the values of reaction rate constant (k) and correlation coefficient (R^2) for photocatalytic reduction of Cr(VI) over the samples. Note: C_{i0} and C_{it} were the Cr(VI) concentration at the irradiation time of 0 and t minutes, respectively.

driven photocatalytic activity in the reduction of aqueous Cr(VI). To quantitatively compare the photocatalytic activities of g-C_3N_4, g-C_3N_4-1, g-C_3N_4-2 and g-C_3N_4-3, the reaction rate constant (k) of photocatalytic Cr(VI) reduction over each sample was obtained by employing the pseudo-first-order kinetic model [62–66]:

$$\ln\left(\frac{C_{i0}}{C_{it}}\right) = kt$$

where C_{i0} and C_{it} were the Cr(VI) concentration at the irradiation time of 0 and t minutes, respectively. The plots of $\ln(C_{i0}/C_{it})$ vs irradiation time (t) and the obtained values of k and correlation coefficient (R^2) for photocatalytic reduction of Cr(VI) over different samples are provided in Fig. 7(b). As can be observed from Fig. 7(b), the order of the k values for photocatalytic reduction of Cr(VI) over different samples was g-C_3N_4-3 > g-C_3N_4-2 > g-C_3N_4-1 > g-C_3N_4. This meant that the hydrothermal treatment in HNO_3 aqueous solution can also enhance the photocatalytic activity of g-C_3N_4 in the reduction of aqueous Cr(VI) under visible-light (wavelength >420 nm) irradiation. Moreover, with the increase of the concentration of HNO_3 aqueous solution used for the hydrothermal treatment, the photocatalytic reduction activity of the resultant g-C_3N_4 became higher.

Fig. 8(a) shows the dark adsorption and visible-light (wavelength >420 nm)-driven photocatalytic reduction of Cr(VI) over the samples obtained from hydrothermal treatment of g-C_3N_4 in 7.6 mol/L HNO_3 aqueous solution at 80, 100 and 120 °C for 12 h, whereas Fig. 8(b) shows the dark adsorption and visible-light (wavelength >420 nm)-driven photocatalytic reduction of Cr(VI) over the samples obtained from hydrothermal treatment of g-C_3N_4 in 7.6 mol/L HNO_3 aqueous solution at 120 °C for 3, 6 and 12 h. As can be observed from Fig. 8(a) and (b), the Cr(VI) adsorption capacity of the hydrothermally treated g-C_3N_4 became larger with the increase of hydrothermal temperature or the extension of hydrothermal time, while the other conditions were the same. The Cr(VI) adsorption capacities of the g-C_3N_4 treated at the hydrothermal temperature of 80, 100 and 120 °C were 40.3%, 70.4% and 77.2%, respectively; whereas the Cr(VI) adsorption capacities of the g-C_3N_4 treated using the hydrothermal time of 3, 6 and 12 h were 70.8%, 73.8% and 77.2%, respectively. Besides, by employing the pseudo-first-order kinetic model, the k values of photocatalytic Cr(VI) reduction over the g-C_3N_4 treated at the hydrothermal temperature of 80, 100 and 120 °C were obtained to be 0.0080, 0.0119 and 0.0189 min^{-1} (Fig. 8(c)), respectively; whereas the k values of photocatalytic Cr(VI) reduction over the g-C_3N_4 treated using the hydrothermal time of 3, 6 and 12 h were obtained to be 0.0105, 0.0137 and 0.0189 min^{-1} (Fig. 8(d)), respectively. Thus, the visible-light-driven photocatalytic Cr(VI) reduction activity of the hydrothermally treated g-C_3N_4 was also enhanced with the increase of hydrothermal temperature or the extension of hydrothermal time, while the other conditions were the same.

The above results demonstrated that the Cr(VI) adsorption and photocatalytic reduction activity of g-C_3N_4 can be tremendously enhanced by hydrothermal treatment in 1.9–7.6 mol/L of HNO_3 aqueous solutions at 80–120 °C for 3–12 h. The enhanced Cr(VI) adsorption of the hydrothermally treated g-C_3N_4 may be mainly ascribed to their larger specific surface areas and positive surface charges, considering the aforementioned characterization results of their structures and other physiochemical properties. However, the higher photocatalytic Cr(VI) reduction activity of the hydrothermally treated g-C_3N_4 was not only resulted from their smaller particle sizes, larger specific surface areas, enhanced adsorption for Cr(VI), and more efficient separation of photogenerated electrons and holes, but also related with the change in the photocatalytic Cr(VI) reduction mechanism as discussed below.

Previous studies had demonstrated that the photocatalytic reduction of Cr(VI) over g-C_3N_4 was dominantly through a two-step superoxide ions($^{\bullet}O_2^-$) mediated indirect reduction mechanism [67,68], that is, first, the photogenerated electrons (e^-) of g-C_3N_4 under visible-light irradiation reduce the adsorbed O_2 to produce $^{\bullet}O_2^-$, then, the $^{\bullet}O_2^-$ reduces Cr(VI). Meanwhile, the reduction of Cr(VI) directly by the e^- of g-C_3N_4 can also take place, but plays only a minor role [67,68]. However, in this study, the hydrothermal treatment in HNO_3 aqueous solution had changed the surface charge of g-C_3N_4 from negative to positive (for example, the Zeta potentials of g-C_3N_4 and g-C_3N_4-3 were –11.9 and +40.7 mV, respectively). As expected, the positively charged surface of the hydrothermally treated g-C_3N_4 would prefer to adsorb the negatively charged Cr(VI) in the form of mainly $Cr_2O_7^{2-}$anions rather than the neutral O_2, whereas the negatively charged g-C_3N_4 would prefer to adsorb the neutral O_2 rather than the negatively charged $Cr_2O_7^{2-}$anions (for example, the Cr(VI) adsorption capacities of g-C_3N_4 and g-C_3N_4-3 were 1.5% and 77.2%, respectively). It was reasonable to relate the more adsorption of Cr(VI) with the less adsorption of O_2, because Cr(VI) and O_2 should compete for the adsorption sites on the surface of the hydrothermally treated g-C_3N_4. Therefore, it was deduced that the Cr(VI) adsorption would occupy the active sites of the hydrothermally treated g-C_3N_4 to inhibit the adsorption of O_2. The less O_2 adsorption would inhibit the subsequent trapping of e^- by O_2 to produce $^{\bullet}O_2^-$, rendering the reduction of Cr(VI) by $^{\bullet}O_2^-$ less possible. To confirm this experimentally, the role of O_2 in the photocatalytic reduction of Cr(VI) over g-C_3N_4 and g-C_3N_4-3 was studied through the contrast experiments in air and N_2 ambient. It can be observed from Fig. 9 that

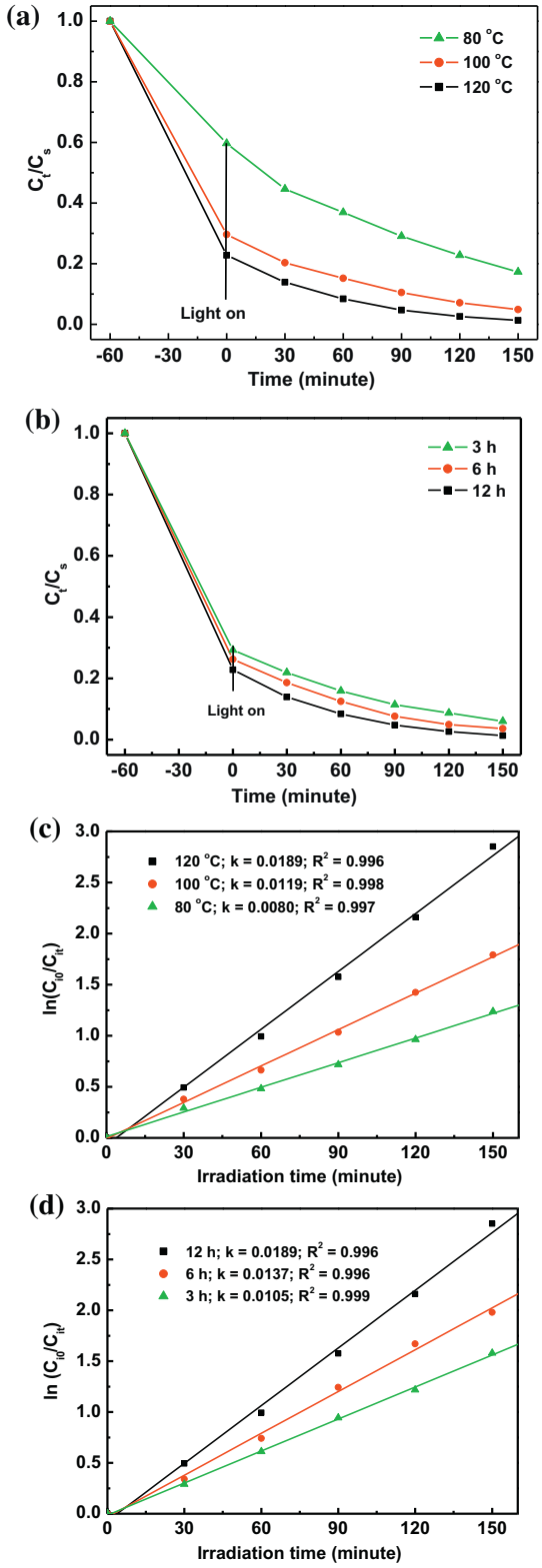

Fig. 8. (a) Dark adsorption and visible-light (wavelength >420 nm)-driven photocatalytic reduction of Cr(VI) over the samples obtained from hydrothermal treatment of g-C_3N_4 in 7.6 mol/L HNO_3 aqueous solution at 80, 100 and 120 °C for 12 h. (b) Dark adsorption and visible-light (wavelength >420 nm)-driven photocatalytic reduction of Cr(VI) over the samples obtained from hydrothermal treatment of g-C_3N_4 in 7.6 mol/L HNO_3 aqueous solution at 120 °C for 3, 6 and 12 h. (c) Plots of $\ln(C_{i0}/C_{it})$ vs irradiation time (t) to obtain the values of reaction rate constant (k) and correlation coefficient (R^2) for photocatalytic reduction of Cr(VI) over the samples obtained from hydrothermal treatment of g-C_3N_4 in 7.6 mol/L HNO_3 aqueous solution at 80, 100 and 120 °C for 12 h. (d) Plots of $\ln(C_{i0}/C_{it})$ vs irradiation time (t) to obtain the values of reaction rate constant (k) and correlation coefficient (R^2) for photocatalytic reduction of Cr(VI) over the samples obtained from hydrothermal treatment of g-C_3N_4 in 7.6 mol/L HNO_3 aqueous solution at 120 °C for 3, 6 and 12 h.

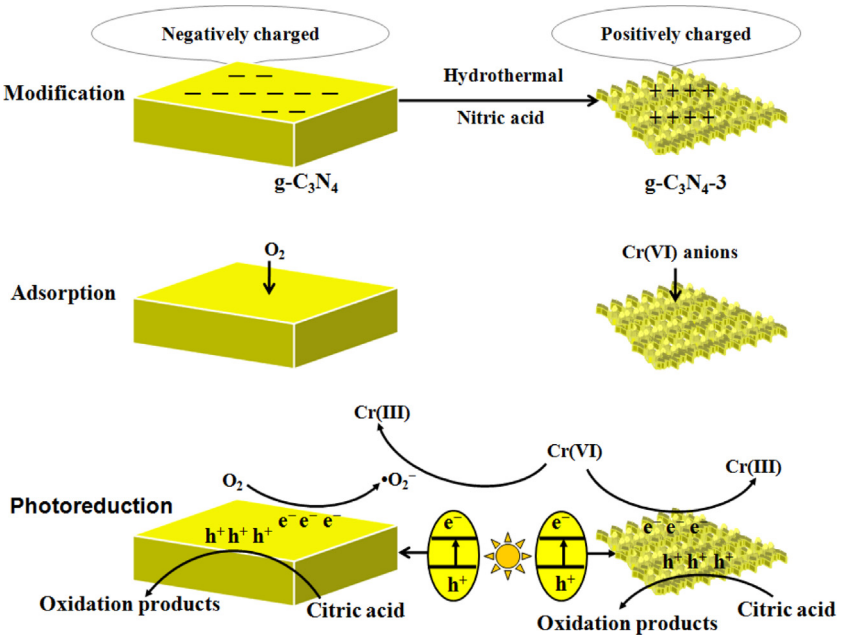

Scheme 1. Mechanisms for the photocatalytic reduction of Cr(VI) over g-C_3N_4 and the hydrothermally treated g-C_3N_4 (taking g-C_3N_4-3 as an example).

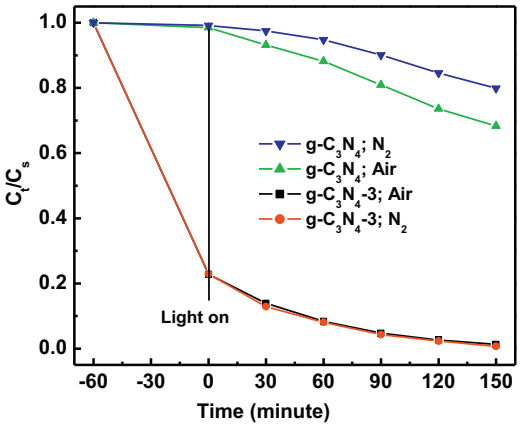

Fig. 9. Comparison of the visible-light (wavelength >420 nm)-driven photocatalytic reduction of Cr(VI) over g-C_3N_4 and g-C_3N_4-3 in air and N_2 ambient.

the photocatalytic reduction of Cr(VI) over g-C_3N_4 in N_2 ambient was obviously suppressed, suggesting that O_2 was involved in the photocatalytic reduction of Cr(VI) over g-C_3N_4 [67,68]. By contrast, the photocatalytic reduction of Cr(VI) over g-C_3N_4-3 was hardly affected after the elimination of O_2 by bubbling high-purity N_2 (Fig. 9), suggesting that O_2 had little to do with the photocatalytic reduction of Cr(VI) over g-C_3N_4-3. Thus, it can be concluded that the two-step $•O_2^-$ mediated indirect reduction governed the photocatalytic reduction of Cr(VI) over g-C_3N_4, but the one-step direct e^- reduction dominated the photocatalytic reduction of Cr(VI) over the hydrothermally treated g-C_3N_4 (for example, g-C_3N_4-3). On the other hand, the photogenerated holes of both g-C_3N_4 and g-C_3N_4-3 were consumed by the oxidation of the sacrificial agent, citric acid (our experiments also demonstrated that tartaric acid, oxalic acid and formic acid can replace citric acid as the sacrificial agent) [69]. The mechanisms for the photocatalytic reduction of Cr(VI) over g-C_3N_4 and the hydrothermally treated g-C_3N_4 (taking g-C_3N_4-3 as an example) are indicated in Scheme 1. Generally, one-step direct reduction can occur more rapidly than two-step indirect reduction kinetically [67]. Accordingly, the photocatalytic reduction of Cr(VI) over the hydrothermally treated g-C_3N_4 was faster.

Fig. 10 shows the XPS spectra of g-C_3N_4-3 recovered after use in the photocatalytic reduction of aqueous Cr(VI) (g-C_3N_4-3-AU). The survey XPS spectrum of g-C_3N_4-3-AU revealed the presence of C, N, O and Cr elements. The C 1s XPS spectrum of g-C_3N_4-3-AU can be deconvoluted into three peaks at 284.8, 288.1 and 289.3 eV, whereas its N 1s XPS spectrum can be deconvoluted into four peaks at 398.7, 400.0, 400.8 and 406.5 eV, respectively. The C 1s and N 1s XPS spectra of g-C_3N_4-3-AU were nearly identical to those of g-C_3N_4-3, suggesting the chemical states of the C and N components of g-C_3N_4-3 remained almost unchanged after photocatalytic use. The O 1s peak of g-C_3N_4-3-AU shifted to lower binding energy (531.8 eV), compared with that (532.2 eV) of g-C_3N_4-3. This was probably because of the presence of Cr(III)-O species on the surface of g-C_3N_4-3-AU. The Cr $2p_{3/2}$ and Cr $2p_{1/2}$ peaks of g-C_3N_4-3-AU were observed at the binding energies of 576.9 and 586.6 eV, respectively, which can be assigned to Cr(III) [49,70]. Thus, Cr(VI) had been reduced to Cr(III) through the photocatalytic reactions mediated by g-C_3N_4-3.

4. Conclusions

The Cr(VI) adsorption and photocatalytic reduction activity of g-C_3N_4 can be enhanced by hydrothermal treatment in HNO_3 aqueous solution. Moreover, larger concentration of HNO_3 aqueous solution, higher hydrothermal temperature, and longer treatment time resulted in higher Cr(VI) adsorption and photocatalytic reduction activity of the hydrothermally treated g-C_3N_4. The larger specific surface areas and positive surface charges of the hydrothermally treated g-C_3N_4 were considered to take the main responsibility for their improved Cr(VI) adsorption. The higher visible-light-driven photocatalytic activity of the hydrothermally treated g-C_3N_4 in Cr(VI) reduction was not only resulted from their smaller particle sizes, larger specific surface areas, enhanced adsorption for Cr(VI), and more efficient separation of photogenerated electrons and holes, but also related with the change in the photocatalytic Cr(VI) reduction mechanism (the photocatalytic reduction of Cr(VI) over g-C_3N_4 was mainly through a two-step $•O_2^-$ mediated indirect reduction mechanism, whereas the photocatalytic reduction of Cr(VI) over the hydrothermally treated g-C_3N_4 was through a one-step direct e^- reduction mechanism).

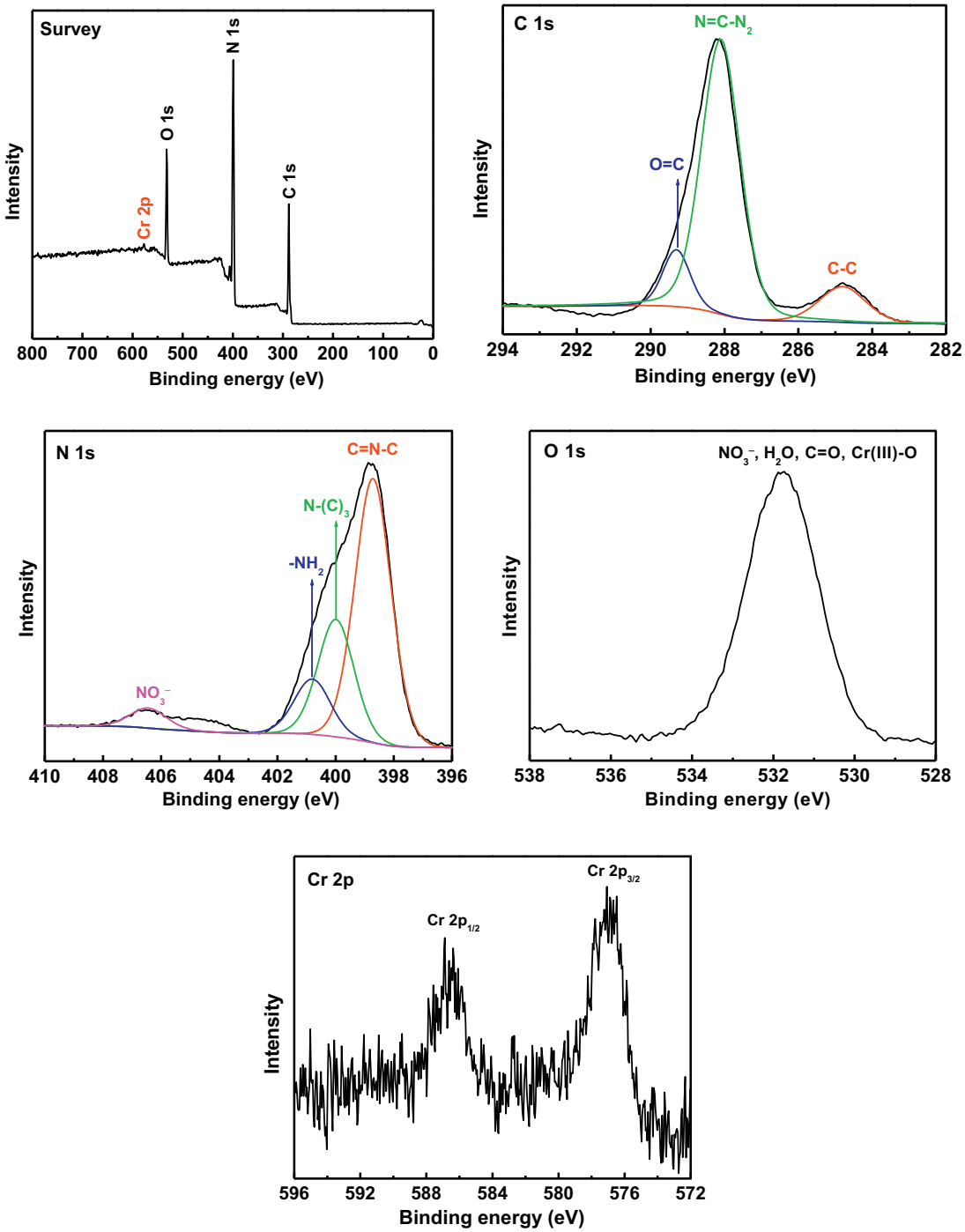

Fig. 10. XPS spectra of g-C_3N_4-3-AU (g-C_3N_4-3 recovered after use in the photocatalytic reduction of aqueous Cr(VI)).

The proposed hydrothermal treatment is a simple and effective way to improve the photocurrent, Cr(VI) adsorption and photocatalytic reduction activity of g-C_3N_4. The hydrothermally treated g-C_3N_4 has great potential for applications in solar energy conversion and environment purification.

Acknowledgements

Thanks to The High Level Talents Foundation of Qingdao Agricultural University (631309), Science and Technology Cooperation Funds of Yangzhou City and Yangzhou University (2014-3), National Natural Science Foundation of China (21475116), College and University Key Project of Jiangsu Province (14KJA430006), Prospective United Innovation Project of Jiangsu Province (SBY2014020171) and The Priority Academic Program Development of Jiangsu Higher Education Institutions. We were also grateful to The Testing Center of Yangzhou University for the XPS, SEM and TEM characterization.

References

[1] Y.C. Zhang, M. Yang, G. Zhang, D.D. Dionysiou, Appl. Catal. B 142–143 (2013) 249–258.
[2] M.I. Litter, Adv. Chem. Eng. 36 (2009) 37–67.
[3] Q. Cheng, C. Wang, K. Doudrick, C.K. Chan, Appl. Catal. B 176–177 (2015) 740–748.

[4] Y. Zhao, Y. Zhang, J. Li, Y. Chen, Sep. Purif. Technol. 129 (2014) 90–95.
[5] J.M. Meichtry, C. Colbeau-Justin, G. Custo, M.I. Litter, Catal. Today 224 (2014) 236–243.
[6] J.M. Meichtry, C. Colbeau-Justin, G. Custo, M.I. Litter, Appl. Catal. B 144 (2014) 189–195.
[7] A. Kleiman, A. Márquez, M.L. Vera, J.M. Meichtry, M.I. Litter, Appl. Catal. B 101 (2011) 676–681.
[8] C. Wang, M. Cao, P. Wang, Y. Ao, J. Hou, J. Qian, Appl. Catal. A 473 (2014) 83–89.
[9] A.E. Giannakas, E. Seristatidou, Y. Deligiannakis, I. Konstantinou, Appl. Catal. B 132–133 (2013) 460–468.
[10] A.E. Giannakas, M. Antonopoulou, Y. Deligiannakis, I. Konstantinou, Appl. Catal. B 140–141 (2013) 636–645.
[11] Y. Yang, G. Wang, Q. Deng, D.H.L. Ng, ACS Appl. Mater. Interfaces 6 (2014) 3008–3015.
[12] G. Moussavi, F. Jiani, S. Shekoohiyan, Sep. Purif. Technol. 151 (2015) 218–224.
[13] H. Li, T. Wu, B. Cai, W. Ma, Y. Sun, S. Gan, Appl. Catal. B 164 (2015) 344–351.
[14] Y.C. Zhang, L. Yao, G. Zhang, D.D. Dionysiou, Appl. Catal. B 144 (2014) 730–738.
[15] J. Zhu, P. Xiao, H. Li, S.A.C. Carabineiro, ACS Appl. Mater. Interfaces 6 (2014) 16449–16465.
[16] Q. Gu, Y. Liao, L. Yin, J. Long, X. Wang, C. Xue, Appl. Catal. B 165 (2015) 503–510.
[17] K. Li, S. Gao, Q. Wang, H. Xu, Z. Wang, B. Huang, ACS Appl. Mater. Interfaces 7 (2015) 9023–9030.
[18] J. Zhang, Y. Chen, X. Wang, Energy Environ. Sci. 8 (2015) 3092–3108.
[19] F. Dong, Z. Wang, Y. Li, W. Ho, Environ. Sci. Technol. 48 (2014) 10345–10353.
[20] T. Sano, S. Tsutsui, K. Koike, T. Hirakawa, Y. Teramoto, N. Negishi, J. Mater. Chem. A 1 (2013) 6489–6496.
[21] F. Dong, Z. Zhao, T. Xiong, ACS Appl. Mater. Interfaces 5 (2013) 11392–11401.
[22] H. Wang, Y. Su, H. Zhao, H. Yu, Environ. Sci. Technol. 48 (2014) 11984–11990.
[23] K. Wang, Q. Li, B. Liu, B. Cheng, W. Ho, J. Yu, Appl. Catal. B 176–177 (2015) 44–52.
[24] Y. He, L. Zhang, B. Teng, M. Fan, Environ. Sci. Technol. 49 (2015) 649–656.
[25] F. He, G. Chen, Y. Yu, S. Hao, ACS Appl. Mater. Interfaces 6 (2014) 7171–7179.
[26] J. Qin, S. Wang, H. Ren, Y. Hou, X. Wang, Appl. Catal. B 179 (2015) 1–8.
[27] L. Cao, R. Wang, D. Wang, Mater. Lett. 149 (2015) 50–53.
[28] M. Zhang, J. Xu, R. Zong, Y. Zhu, Appl. Catal. B 147 (2014) 229–235.
[29] D. Zheng, C. Pang, Y. Liu, X. Wang, Chem. Commun. 51 (2015) 9706–9709.
[30] C. Huang, C. Chen, M. Zhang, L. Lin, X. Ye, S. Lin, M. Antonietti, X. Wang, Nat. Commun. 6 (2015) 7698–7705.
[31] G. Zhang, M. Zhang, X. Qiu, X. Wang, Adv. Mater. 26 (2014) 805–809.
[32] J. Zhang, M. Zhang, C. Yang, X. Wang, Adv. Mater. 26 (2014) 4121–4126.
[33] Y. Chen, B. Wang, S. Lin, Y. Zhang, X. Wang, J. Phys. Chem. C 118 (2014) 29981–29989.
[34] J. Sun, J. Zhang, M. Zhang, M. Antonietti, X. Fu, X. Wang, Nat. Commun. 3 (2012) 1139–1146.
[35] B. Shen, Z. Hong, Y. Chen, B. Lin, B. Gao, Mater. Lett. 118 (2014) 208–211.
[36] M. Zhang, X. Wang, Energy Environ. Sci. 7 (2014) 1902–1906.
[37] S. Chen, C. Wang, B.R. Bunes, Y. Li, C. Wang, Appl. Catal. A 498 (2015) 63–68.
[38] H. Li, J. Liu, W. Hou, N. Du, R. Zhang, Appl. Catal. B 160–161 (2014) 89–97.
[39] Z. Jin, N. Murakami, T. Tsubota, T. Ohno, Appl. Catal. B 150–151 (2014) 479–485.
[40] Y. Zhang, A. Thomas, M. Antonietti, X. Wang, J. Am. Chem. Soc. 131 (2009) 50–51.
[41] J. Zhang, M. Zhang, L. Lin, X. Wang, Angew. Chem. Int. Ed. 54 (2015) 6297–6301.
[42] J. Xu, L. Zhang, R. Shi, Y. Zhu, J. Mater. Chem. A 1 (2013) 14766–14772.
[43] Y. Zhang, Q. Zhang, Q. Shi, Z. Cai, Z. Yang, Sep. Purif. Technol. 142 (2015) 251–257.
[44] W. Ho, Z. Zhang, M. Xu, X. Zhang, X. Wang, Appl. Catal. B 179 (2015) 106–112.
[45] H. Zhao, H. Yu, X. Quan, Appl. Catal. B 152–153 (2014) 46–50.
[46] L. Ye, J. Liu, Z. Jiang, T. Peng, L. Zan, Appl. Catal. B 142–143 (2013) 1–7.
[47] M. Tahir, C. Cao, F.K. Butt, J. Mater. Chem. A 1 (2013) 13949–13955.
[48] R.C. Pawar, Y. Pyo, S.H. Ahn, C.S. Lee, Appl. Catal. B 176 (2015) 654–666.
[49] J.F. Moulder, W.F. Stickle, P.E. Sobol, K.D. Bomben, Handbook of X-Ray Photoelectron Spectroscopy, in: J. Chastain (Ed.), PerkinElmer Corporation, Eden Prairie, 1992.
[50] J. Xu, Y. Wang, Y. Zhu, Langmuir 29 (2013) 10566–10572.
[51] Y. Yang, Y. Guo, F. Liu, X. Yuan, Y. Guo, Appl. Catal. B 142–143 (2013) 828–837.
[52] Y. Zheng, L. Lin, X. Ye, F. Guo, X. Wang, Angew. Chem. Int. Ed. 53 (2014) 11926–11930.
[53] S. Kang, Y. Fang, Y. Huang, L. Cui, Y. Wang, Appl. Catal. B 168–169 (2015) 472–482.
[54] Q. Lin, L. Li, S. Liang, Appl. Catal. B 163 (2015) 135–142.
[55] H. Sun, G. Zhou, Y. Wang, A. Suvorova, ACS Appl. Mater. Interfaces 6 (2014) 16745–16754.
[56] B. Zhao, W. Sun, W. Ren, Y. Huang, Z. Li, J. Solid State Chem. 206 (2013) 91–98.
[57] X. Wang, S.O. Pehkonen, A.K. Ray, Ind. Eng. Chem. Res. 43 (2004) 1665–1672.
[58] J. Zhanga, Y. Hu, X. Jiang, S. Chen, J. Hazard. Mater. 280 (2014) 713–722.
[59] G. Wu, S.S. Thind, J. Wen, K. Yan, A. Chen, Appl. Catal. B 142–143 (2013) 590–597.
[60] Y. Zang, L. Li, X. Li, R. Lin, G. Li, Chem. Eng. J. 246 (2014) 277–286.
[61] K. Sridharan, E. Jang, T.J. Park, Appl. Catal. B 142–143 (2013) 718–728.
[62] H. Xu, J. Yan, Y. Xu, Y. Song, H. Li, Appl. Catal. B 129 (2013) 182–193.
[63] Y.C. Zhang, J. Li, H.Y. Xu, Appl. Catal. B 123–124 (2012) 18–26.
[64] R. Lu, P. Fang, X. Liu, S. Zhai, C. Li, X. Zhao, Appl. Catal. B 179 (2015) 558–573.
[65] G. Dong, K. Zhao, L. Zhang, Chem. Commun. 48 (2012) 6178–6180.
[66] W. Zhao, Z. Wei, H. He, J. Xu, J. Li, S. Yang, C. Sun, Appl. Catal. A 501 (2015) 74–82.
[67] G. Dong, L. Zhang, J. Phys. Chem. C 117 (2013) 4062–4068.
[68] X. Hu, H. Ji, F. Chang, Y. Luo, Catal. Today 224 (2014) 34–40.
[69] L. Yang, Y. Xiao, S. Liu, Y. Li, Q. Cai, S. Luo, Appl. Catal. B 94 (2010) 142–149.
[70] J. Wu, J. Wang, Y. Du, H. Li, Y. Yang, Appl. Catal. B 174–175 (2015) 435–444.